

Alma Mater Studiorum Università di Bologna  
Archivio istituzionale della ricerca

Anodizing of AA6082-T5 by conventional and innovative treatments: Microstructural characterization and dry sliding behaviour

This is the final peer-reviewed author's accepted manuscript (postprint) of the following publication:

*Published Version:*

Sola R., Tonelli L., Shashkov P., Bogdanoff T.H., Martini C. (2020). Anodizing of AA6082-T5 by conventional and innovative treatments: Microstructural characterization and dry sliding behaviour. WEAR, 458-459, 1-13 [10.1016/j.wear.2020.203423].

*Availability:*

This version is available at: <https://hdl.handle.net/11585/784272> since: 2021-05-24

*Published:*

DOI: <http://doi.org/10.1016/j.wear.2020.203423>

*Terms of use:*

Some rights reserved. The terms and conditions for the reuse of this version of the manuscript are specified in the publishing policy. For all terms of use and more information see the publisher's website.

This item was downloaded from IRIS Università di Bologna (<https://cris.unibo.it/>).  
When citing, please refer to the published version.

(Article begins on next page)

This is the final peer-reviewed accepted manuscript of:

R. Sola, L. Tonelli, P. Shashkov, T.H. Bogdanoff, C. Martini. Anodizing of AA6082-T5 by conventional and innovative treatments: Microstructural characterization and dry sliding behaviour, Wear 458–459 (2020) 203423.

The final published version is available online at:

<https://doi.org/10.1016/j.wear.2020.203423>:

Rights / License: CC-BY-NC-ND 4.0 license

(<http://creativecommons.org/licenses/by-nc-nd/4.0/>)

The terms and conditions for the reuse of this version of the manuscript are specified in the publishing policy. For all terms of use and more information see the publisher's website.

*This item was downloaded from IRIS Università di Bologna (<https://cris.unibo.it/>)*

***When citing, please refer to the published version.***

# Anodizing of AA6082-T5 by conventional and innovative treatments: microstructural characterization and dry sliding behaviour

R. Sola<sup>a\*</sup>, L. Tonelli<sup>a</sup>, P. Shashkov<sup>b</sup>, T.H. Bogdanoff<sup>c</sup>, C. Martini<sup>a</sup>

<sup>a</sup>*Department of Industrial Engineering, University of Bologna, viale Risorgimento 4, 40136, Bologna, Italy*

<sup>b</sup>*Cambridge Nanolitic Ltd, 3b Homefield Road, Haverhill, Suffolk, CB9 8QP, UK*

<sup>c</sup>*School of Engineering, Jönköping University, Box 1026, 55111 Jönköping, Sweden*

Corresponding author: Dr. Ramona Sola, *Department of Industrial Engineering, University of Bologna, viale Risorgimento 4, 40136, Bologna, Italy* ([ramona.sola@unibo.it](mailto:ramona.sola@unibo.it))

## Abstract

This work focuses on the comparison of microstructure and tribological behaviour (dry sliding vs. 100Cr6 steel) of anodic layers produced on wrought AA6082-T5 by hard anodizing (HA), plasma electrolytic oxidation (PEO, sometimes also termed MAO, Micro-Arc Oxidation) and novel electrochemical oxidation (ECO), derived from PEO minimising its disruptive plasma discharge. The results showed that PEO and HA do not decrease the coefficient of friction of AA6082, whilst ECO does (particularly after sealing with a phosphate-based solution), thanks to its smooth surface and decreased stability of Fe-O based transfer layers. All the anodizing treatments improve wear resistance of AA6082: ECO showed the highest wear resistance, due to the beneficial combination of compact microstructure, high and uniform thickness, high microhardness and adhesion.

## Keywords

Sliding wear, Non-ferrous metals, Other surface engineering processes, Electron microscopy, Profilometry, Scratch testing

## 1. Introduction

Aluminium alloys are used for an increasing range of engineering applications, due to their many advantages (high strength-to-weight ratio, high electrical and thermal conductivity, good formability and, last but not least, recyclability [1]). Even though these alloys are attracting a growing interest in sectors such as the packaging industry, their unsatisfactory tribological behaviour still remains a critical issue for many applications. Several surface engineering techniques, such as physical vapour deposition (PVD), plating/electroplating, anodizing, thermal spraying and laser-based surface treatments [2,3] are available to improve the tribological behaviour of aluminium alloys. For many decades, the conventional and most cost-effective solution to wear problems has been Hard Anodizing (HA). However, since the beginning of this century, Plasma Electrolytic Oxidation (PEO) has become an attractive alternative to conventional anodizing. PEO is an electrochemical conversion treatment, based on the modification of the growing anodic oxide by micro-discharges, initiated at potentials above the breakdown voltage [4], sometimes also termed Micro-Arc Oxidation (MAO). Several comparative studies have been published on PEO and HA [5-8] and the main advantages of PEO over HA can be summarised as follows: (i) use of dilute alkaline electrolytic baths instead of concentrated acidic solutions; (ii) higher thickness, hardness, practical adhesion and wear resistance of PEO layers, with possible incorporation of anions from the bath; (iii) higher tolerance towards alloying elements such as Cu and Si than the conventional hard anodizing process. All these features are related to specific PEO treatment conditions, derived from conventional anodizing but involving higher voltages (above dielectric breakdown of the anodic oxide) so as to generate micro-arc discharges which assist and enhance the growth of oxide-based layers. However, from a tribological point of view, also PEO has a few disadvantages: (i) heterogeneous microstructure with micropores

and cracks, mostly in the outer “technological” layer, which may induce micro-crack driven damage and coating removal in the form of flakes [9] (ii) a high roughness in the as-treated condition, generating relatively high friction against steel counterparts in dry sliding conditions [10], therefore requiring a grinding/polishing post-treatment, applicable only when part geometry is not too complex.

The microstructure of anodic layers grown by PEO can be optimised by controlling electrolyte composition, concentration, pH and temperature as well as electrical parameters (power source, current regime) [9]. The use of AC and DC-pulsed sources remarkably contributed to the development of PEO layers with improved tribological behaviour. In particular, bipolar pulse sources are able to produce dense and compact coatings, whilst when only positive pulses are applied, the oxide-based layer displays a porous morphology [11]. Based on the above considerations, a novel anodizing treatment has been developed in an industrial environment. The treatment, termed Electro-Chemical Oxidation (ECO), derives from PEO but minimises or avoids its disruptive plasma discharge effects (UK Patent GB2497063, Cambridge Nanolitic Ltd). It was achieved by (1) using short (microseconds) electrical pulses with trapezoidal shape to reduce the electrical current peaks during pulse switching and (2) maintaining cathodic current at a level that secures cathodic etching and building oxide layer with a fine nanopore structure to facilitate charge and ion transfer to the oxidation zone and to avoid breakdown discharge.

Although ECO coatings have already found application in a number of industries such as textile, packaging and automotive, their properties have not been published yet: this work focuses on the comparison of microstructure and tribological behaviour of ECO, PEO and HA coatings produced on the wrought AA6082-T5 aluminium alloy. The main aim of this work is therefore to provide a comparison of the anodic layers obtained by these industrial anodizing processes, which will help in process selection for a given industrial application. It will also allow a deeper understanding of microstructural features and tribological behaviour of the layers produced by each investigated process.

## 2. Materials and Methods

The wrought AA6082 alloy, used as substrate for all the investigated anodizing treatments was provided in the T5 condition, in the form of small bars (10x10x70 mm<sup>3</sup>). The T5 heat treatment consisted of (i) extrusion at 527°C, (ii) quenching in water and (iii) aging at 177 °C for 8 h. The chemical composition of AA6082, determined by Glow Discharge Optical Emission Spectroscopy (GDOES), is reported in Table 1. No deviations from nominal composition data [12] were observed.

Before each anodizing treatment, AA6082 samples were polished by standard metallographic techniques and then degreased in ultrasonicated acetone. Anodizing treatments were carried out in an industrial environment either by conventional Hard Anodizing (HA) or by Plasma Electrolytic Oxidation (PEO) or by Electro-Chemical Oxidation (ECO). The main features of each treatment are summarized and compared in Table 2.

The comparison of features in Table 2 shows that the investigated treatments differ in terms of voltage and current density (both PEO and ECO work above dielectric breakdown, while HA remains below it). Though the ECO process makes use of higher currents and voltages than PEO, its energy consumption per  $\mu\text{m}$  of coating growth is lower, because ECO is faster and more energy efficient, building a higher thickness per unit of energy consumed. ECO energy efficiency is explained by the fact that ECO is not consuming significant energy for creating electric discharges across oxide dielectric layer. It is achieved by maintaining an optimal ratio between anodic and cathodic pulse



currents so that cathodic pulse etching effect provides a dynamic nanopore structure for the growing oxide film to facilitate charge and ion transfer to the oxidation zone and minimise electrical breakdown discharge effect. Moreover, both PEO and ECO use alkaline solutions instead of the concentrated acidic bath typically used in HA.

All the processes were conducted so as to produce oxide layers about 50  $\mu\text{m}$  thick. Actual thicknesses were measured by image analysis of polished cross-sections (averaging data obtained by at least 5 measurements at the same magnification). ECO layers were investigated both in the as-treated condition and after sealing by immersion in a phosphate-based solution.

### 2.1 Microstructural and mechanical characterization

Microstructural characterization of the untreated AA6082-T5 alloy was carried out by standard metallographic techniques, using Keller's reagent (1 mL HF, 1.5 mL HCl, 2.5 mL HNO<sub>3</sub>, 95 mL H<sub>2</sub>O) for highlighting the microstructure. The chemical composition of the alloy was checked by Glow Discharge Optical Emission Spectroscopy (GDOES) with a Grimm-style glow discharge lamp in DC mode (Spectrums Analytik GDA 650). The analysed area in each measurement was about 5 mm<sup>2</sup>, corresponding to the internal area of the tubular anode (2.5 mm diameter).

Surface and cross-sectional observations of the anodized samples were carried out by scanning electron microscopy (SEM, Zeiss EVO 50) in low vacuum mode.

The phase constitution of the PEO layers was determined by X-ray diffraction (XRD), performing  $\theta$ - $2\theta$  scans from 10° to 100° with a 0.02 step size and a 4 s dwell time, by a PANalytical Expert PRO X-ray diffractometer with Xcelerator detector and a Ni-filtered Cu-K $\alpha$  radiation source ( $\lambda = 0.15405$  nm), operated at 40 kV and 30 mA. Semiquantitative determination of  $\alpha$ - and  $\gamma$ -Al<sub>2</sub>O<sub>3</sub> in the oxide layers was carried out by comparing the integrated diffraction intensities of the (113) $\alpha$  peak ( $2\theta=43.4^\circ$ ) and the (400) $\gamma$  peak ( $2\theta=45.7^\circ$ ), according to the method proposed by [1]. Integrated intensities were determined by the X'Pert High-Score Plus software (PANalytical).

Topographic measurements were carried out on **the free surface of coatings" (i.e. the as-coated surface, without any post-treatment)** by stylus profilometry (Hommelwerke T2000, radius of curvature of the stylus tip: 5  $\mu\text{m}$ ), in order to measure the surface roughness and characterize surface morphology. Microhardness vs. depth profiles were carried out on polished cross-sections of anodized samples using a Knoop microhardness tester with a load of 100 g (HK<sub>0.1</sub>).

Scratch tests were also carried out on the anodic oxides, using a Revetest device (CSM Instruments) equipped with a Rockwell diamond indenter (spherical tip radius: 200  $\mu\text{m}$ ). Progressive load scratch tests were carried out from 1 to 100 N, with a linear speed rate of 10 mm min<sup>-1</sup> and a scratch length of 10 mm. Scratches morphology was observed by optical microscopy during scratching and by 3-D digital microscopy and SEM after scratching.

### 2.3 Dry sliding tests

Dry sliding tests were carried out on untreated AA6082-T5 as well as on the anodized alloy (PEO, ECO or HA, Table 1) using a flat-on-cylinder tribometer (block-on-ring contact geometry, ASTM G-77 [14]), described in further detail elsewhere [15]. **Stationary anodized samples slid against a rotating 100Cr6 (AISI 52100) bearing steel cylinder (diameter: 40 mm), with a surface hardness of 60 HRC and a roughness  $R_a=0.15 \pm 0.03 \mu\text{m}$ . The counterfacing materials in dry sliding tests was a rotating 100Cr6 (AISI 52100) bearing steel cylinder (diameter: 40 mm), with a surface hardness of 60 HRC and a roughness  $R_a=0.15 \pm 0.03 \mu\text{m}$ . Stationary anodized or untreated samples (flat blocks, 10x10x70 mm<sup>3</sup>) were kept in contact with the rotating cylinder, generating a counterformal line contact.**

All anodized surfaces were tested in the as-treated condition (i.e. not polished), so as to simulate the situation in which grinding or polishing is not applicable due to complex part geometry.

Sliding tests were performed at ambient conditions of temperature and humidity (relative humidity ranging from 50 to 60 %), at fixed sliding speed (0.3 m s<sup>-1</sup>) and under normal loads of 5, 20 and 40 N. These conditions led to Hertzian contact pressures (Tab. 3) estimated according to [16],

considering elastic modulus and Poisson's ratio for prevalent phases in anodic oxides, as determined by XRD.

Friction force values were continuously recorded during each test as a function of sliding distance, by means of a bending load cell. Friction values were averaged over the steady-state regime for each test and then averaged again over the repetitions of each test. After the tests, maximum wear scar depths on sliders and cylinders were separately evaluated by stylus profilometry (tip radius: 5  $\mu\text{m}$ ). Worn surfaces were characterized by Hirox KH 7700 3D-digital microscope and SEM-EDS in order to identify the dominant wear mechanisms. Subsurface damage mechanisms in anodic oxide layers was also investigated by FIB. A position in the wear track was selected in the sliding direction, and a trench with a width of 20  $\mu\text{m}$  was made by rough FIB milling of  $\sim 2 \mu\text{A}$  at 30 keV. Fine polishing of the region of interest was performed using FIB current of  $\sim 100 \text{ nA}$  at 30 keV. The microstructure of the polished section was then observed by high-resolution SEM (LYRA3, TESCAN).

### 3. Results and Discussion

#### 3.1 Surface morphology, microstructure and roughness

Figure 1 shows the free surface morphology (a-c) and the polished cross-sections of all anodized samples (d-n), whilst Table 4 reports surface roughness parameters according to ISO 4278 [17] for the AA6082 substrate and for anodized samples, together with average thickness values of anodic oxides.

The free surfaces of HA (Fig. 1a) showed the typical morphology of hard-anodised layers, with substrate surface features (such as grinding grooves) being closely replicated, as well as the presence of some cracks. Cross-section observation demonstrated that cracks extend through the thickness of the anodic oxide, mostly in the corners of the treated samples (Fig. 1d). Higher magnification observation (Fig. 1g and l) showed some micro-porosities or inclusions scattered across the HA layer, which has a fairly homogeneous thickness of about  $44.6 \pm 0.5 \mu\text{m}$  (Table 4).

The free surface of PEO layers showed the typical volcano-like features, due to the action of electric discharges inducing material rearrangement (i.e. melting-solidification-recrystallisation cycles) inside and around discharge channels [18]. Consequently, also cross-section observation showed a network of surface cracks and micro-defects (Fig. 1h and m), as well as the typical layered microstructure with an inner region characterised by a dense network of micro-channels, and an outer one, which experienced only the last and more energetic discharges and hence appears more extensively cracked.

The above-described PEO microstructure is also responsible for the low thickness homogeneity, highlighted by the highest relative standard deviation (RSD) of thickness values (Table 4).

The ECO layers displayed the smoothest surface (Fig. 1c), due to a very dense microstructure as shown by cross-sections in Figure 1f and i. The ECO layer was characterised by the lowest porosity and the best ability to follow the corner of the sample (Fig. 1f) without developing cracks (conversely to HA, Fig. 1d) or other defects. Moreover, ECO appeared to be very homogeneous and did not show a pronounced multilayered structure (Fig. 1i), conversely to PEO (Fig. 1h). A network of micro-channels near the interface with the substrate was still visible (Fig. 1n), but it was finer and with lower porosity than in PEO (Fig. 1m), due to lower discharge intensity in ECO.

All the oxide layers showed well-bonded coating-substrate interfaces (Fig. 1l-n), with slight interfacial waviness for PEO and ECO, due to localised inward growth assisted by arc micro-discharges. The higher electric discharge control ability of ECO also accounts for the smoother interface, clearly observable by comparing all the cross-sections of ECO and PEO.

Surface roughness parameters in Table 4 are consistent with the above discussed surface morphologies and microstructures: HA closely replicated substrate roughness, PEO increased it and ECO decreased it. It is worth noting that PEO was deliberately not polished so as to simulate the situation in which grinding/polishing is not applicable due to complex part geometry. Table 4 also

reports on the sealed version of ECO, showing that the sealing process does not affect roughness of the ECO layers, which are already very smooth in the as-treated condition.

### 3.2 Elemental composition and phase constitution

EDS X-ray maps of the anodized layers in Figure 2 show that Al and O were the main elements in all the layers. PEO also incorporated some elements from the electrolyte bath such as P and Si (as observed in [9]), whilst HA incorporated S-based anionic species from the electrolyte in the cylindrical nanopores [19]). The sealing post-treatment of ECO layers in phosphate-based solution induced a slight P enrichment in a very thin portion of the outer zone, but no significant contributions from the electrolyte were detected in ECO layers.

XRD patterns, representative of the whole layer thickness (as indicated by the detection of substrate peaks), are reported in Figure 3. Diffraction patterns of HA layers only showed peaks from the underlying AA6082 alloy, due to the amorphous structure of the anodic oxide [20]. Conversely, both ECO and PEO layers mostly consisted of crystalline phases.

In PEO,  $\gamma$ -Al<sub>2</sub>O<sub>3</sub> was the main phase, accompanied by traces of  $\alpha$ - and  $\delta$ -Al<sub>2</sub>O<sub>3</sub>. The  $\alpha$ -Al<sub>2</sub>O<sub>3</sub>/ $\delta$ -Al<sub>2</sub>O<sub>3</sub> ratio, estimated as described in section 2.1, was 0.036. The dominance of metastable  $\gamma$ -Al<sub>2</sub>O<sub>3</sub> in PEO-treated Al-Mg wrought alloys was observed also by other authors [21,22] and can be attributed to rapid quenching after localised discharge events, whilst partial transformation to the stable phase  $\alpha$ -Al<sub>2</sub>O<sub>3</sub> is favoured by high temperature annealing during coating growth [18]. The detection of traces of another transition alumina like  $\delta$ -Al<sub>2</sub>O<sub>3</sub> can be considered a further indication of partial  $\gamma$ -to- $\alpha$  transformation according to the  $\gamma \rightarrow \delta \rightarrow \theta \rightarrow \alpha$  sequence [24].

In ECO layers both  $\alpha$ - and  $\gamma$ -Al<sub>2</sub>O<sub>3</sub> were detected in nearly equal proportion, with a slight predominance of  $\alpha$ . ECO layers therefore also contain higher amounts of  $\alpha$ -Al<sub>2</sub>O<sub>3</sub> by comparison to PEO ( $\alpha$ -Al<sub>2</sub>O<sub>3</sub>/ $\delta$ -Al<sub>2</sub>O<sub>3</sub> ratio for ECO: 1.4), probably due the less intense discharge regime of ECO, which favours gradual thermal transformation to the stable  $\alpha$  phase.

### 3.3 Microhardness and progressive load scratch testing

Knoop micro-hardness measurements recorded along the cross-section of the anodic oxides (Fig. 4) show that all the treatments allow increasing surface hardness of AA6082, which in the untreated condition is about  $120 \pm \text{HK}_{0.1}$  (bulk). The apparent decrease of hardness towards the outer zone of the layers is due to location of indentations near the coating-mounting resin interface, whilst near the coating-substrate interface hardness may be underestimated due to contribution of the substrate.

The highest hardness increase was afforded by the ECO process, due to its compact microstructure (Fig. 1) and the presence of hard  $\alpha$ -Al<sub>2</sub>O<sub>3</sub> as the main phase constituent (Fig. 3). The sealing post-treatment did not affect cross-sectional hardness of ECO layers, due to the very shallow depth of the zone affected by sealing (as shown by EDS X-ray maps in Fig. 2).

The hardness values measured on PEO and HA are slightly lower than those reported in [7], even though similar trends were observed.

PEO layers showed hardness values about 2.5 times higher than HA, due to the beneficial influence of crystalline  $\gamma$ -Al<sub>2</sub>O<sub>3</sub> by comparison to amorphous HA layers. However, the hardness vs. depth trend of PEO layers is less constant than those of ECO and HA, with higher hardness in the outer zone of the PEO layer. This behaviour was observed also by Curran and Clyne [18], who attributed it to the predominance of harder and more stable phases where high temperature annealing prevails on rapid quenching. Conversely, the higher hardness homogeneity across the ECO and HA layers is probably due to the absence (HA) or lower intensity (ECO) of arc discharges, hence to a more homogeneous phase constitution and microstructure.

Figure 5 shows the histogram with critical loads for coating failure ( $L_{c2}$ ) measured by scratch testing, together with representative optical images of scratch tracks for all the anodised layers. Both the PEO and ECO coatings were smoothed inside the track, within which mostly conformal cracks (due to tensile stresses behind the trailing edge of the stylus [24]) were observed, until the onset of

coating failure ( $L_{c2}$ ) followed by total breakthrough ( $L_{c3}$ ). The scratch tracks on ECO coatings were particularly smooth and homogeneous, showing wedge spallation due to compressive stresses ahead of the stylus. The highest  $L_{c2}$  values were measured on ECO layers, due to their dense microstructure, high thickness and low roughness. The sealing post-treatment did not show any beneficial effect on practical adhesion, due to the very superficial localisation of the P-enriched layer (as discussed in section 3.2). Conversely, HA layers showed the lowest  $L_{c2}$  values, undergoing significant chipping before interfacial failure, probably due to the presence of through-thickness cracks already before testing (Fig. 1a,d).

### 3.4 Dry sliding tests

#### 3.4.1 Friction and wear behaviour

Representative coefficient friction (COF) values recorded as a function of sliding distance under a normal load of 5 N are shown in Figure 6 for both the untreated AA6082 alloy and the anodised surfaces. In the steady-state regime, untreated AA6082 slides against 100Cr6 steel with a COF of about 0.4, lower than for treated samples and consistent with literature data [25-28]. Moreover, dynamic COF data of the AA6082/steel couple displayed large oscillations, due to stick-slip phenomena [29]. For PEO, ECO and HA, higher COF values were measured, ranging between 0.6 and 1, as a result of the increase in the abrasive component of friction by comparison to the untreated substrate. This is a well-documented phenomenon for PEO layers, due to the typical combination of high hardness and relatively high roughness in the unpolished condition. In fact, among all anodized layers investigated in this work, PEO exhibited the highest friction values. HA layers showed slightly lower values of dynamic COF than PEO, due to their lower hardness and roughness: however, the COF of HA tends to increase and presents some oscillations, probably due to the onset of micro-cracking phenomena (discussed in section 3.4.2), favoured by the presence of cracks in the HA layers already before sliding. Conversely, the very smooth surface of ECO samples allowed reaching the lowest dynamic friction values, close to those measured for the untreated AA6082.

Average steady-state COFs as a function of normal load are shown in Figure 7. COFs of ECO and PEO are not significantly influenced by applied load, differently from HA and untreated AA6082. The COF of AA6082 slightly increased with normal load, probably due to the abrasive action of fragments detaching from iron oxide transfer layers [25]. At low normal load, HA shows average COF values similar to ECO, but at 20 N the COF started to increase, probably due to more extensive micro-cracking that forms large abrasive fragments, as previously discussed. The high hardness and roughness of PEO caused the highest COFs in all the normal load ranges, due to the previously discussed increase of the abrasive component of friction as well as to material transfer from steel counterpart (i.e. formation of iron oxide-based debris layers, as discussed in section 3.4.2). The lowest roughness and compact microstructure of ECO and sealed ECO coatings yielded the lowest COFs in all the investigated loading condition. In particular, the beneficial influence of sealing in the phosphate-based solution on COF, already observed in dynamic COF vs. sliding distance plots (Fig. 6), was confirmed also by average COF values in Figure 7.

Maximum wear depth values as a function of normal load are shown in Figure 8. All the investigated coatings greatly improved wear resistance of the alloy, as a results of increased surface hardness. On the other hand, severe wear was observed for untreated AA6082 (Fig. 8a), due to extensive ploughing and plastic deformation. The wear depth vs. normal load plots for the anodised layers (Fig. 8b) always showed an increasing trend and could be divided in two groups: (i) PEO and HA, with higher wear depths than (ii) ECO and sealed ECO. The comparable wear depths of PEO and HA are a further demonstration that wear resistance is not affected by hardness alone: the high roughness of unpolished PEO layers is probably the main detrimental factor.

The combination of high hardness, smooth surface, compact microstructure and good adhesion of ECO layers is responsible for their high wear resistance. Comparing maximum wear depth with ECO coating thickness (Table 4), it is possible to notice that the coating was never completely removed

during sliding, under all the investigated loading conditions. The sealing post-treatment did not affect wear behaviour, as expected on the basis of its main features, discussed in previous sections.

Conversely, PEO and HA are slightly thinner and substantially less homogeneous and dense than ECO. Significant stress concentration would be expected at the thinner section for the coatings around micro-cracks and micro-defects. These would lead to premature failure of the coatings compared to ECO, where in-plane stress would be more homogeneously distributed and spread across a wider cross-section.

Lastly, it is important to point out that in all tests, regardless the anodised layer, the wear mechanism of the counter-surface was always mild tribo-oxidation and the wear depth of the counter-surface was not detectable by stylus profilometry.

#### 3.4.2 Wear track morphology

In order to achieve a better understanding of the wear behaviour, wear scar morphology was observed both on the surface (optical images in Fig. 9, SEM images in Fig. 10) and in cross-sections obtained by FIB milling (FEG-SEM images in Fig. 11).

Wear tracks of the untreated AA6082 alloy (Fig. 9) are much wider and deeper than those of anodised samples and display a typical severe adhesive/abrasive wear morphology, with a heavily ploughed metallic surface, only slightly and discontinuously covered by a black transfer layer, mostly consisting of aluminium oxide as indicated by EDS data in Table 5.

Conversely, the wear tracks on PEO, ECO and HA are covered with reddish transfer layers, to an extent that depends on the roughness of each anodised layer ( $PEO > HA > ECO \approx ECO \text{ sealed}$ ). Higher magnification BSE images in Figure 10 show a more detailed view of the wear scar morphologies for all the anodised layers. On PEO, a rather continuous layer (light grey surface in Fig. 10a) cover most of the surface, with a few asperities of the underlying rough coating (dark grey) emerging out of it. EDS analyses carried out on the debris layer demonstrated that it mostly consists of iron oxides (Table 5), deriving from mild tribo-oxidation of the steel counterface. The transfer layer is thick enough to make the signal from Al not detectable. These transfer layers are more stable, hence thick and continuous on PEO, due to its higher surface roughness (Tab. 4). They were observed and discussed also in previous works [30] and probably also contribute to increase friction, as the contact conditions change from “anodic oxide vs. steel” to “iron oxide vs. iron oxide”, when the transfer layer stabilises on both mating surfaces.

Also, HA coatings show the presence of these iron oxide-based transfer layers, even though they are less continuous than on PEO (Fig. 9, Fig. 10b). Where the worn HA coating is not covered by the iron oxide transfer layer, a network of micro-cracks is clearly visible (Fig. 10b), as a result of the propagation and multiplication of the pre-existing cracks during sliding.

The transfer layers, although probably contributing to the high COFs of PEO and HA, could also be slightly wear protective, as already observed for similar layers generated during mild tribo-oxidative wear in several systems [31, 34], even though it does not increase the wear resistance of PEO and HA by comparison to ECO. As the applied load increases, the transfer layer may become instable and start to crack and delaminate, as observed for HA already at 20 N (Fig. 10b), probably also due to the lower load support ability of this anodic oxide by comparison to PEO.

On the other hand, wear tracks on ECO coatings (either sealed or not) are only slightly covered by reddish iron oxides, mostly at the exit side of the track (Fig. 9). BSE images in Figure 10 c and d show only discontinuous and scattered light grey spots on the surface of wear tracks of ECO and sealed ECO respectively. EDS analysis of these spots (Tab. 5) indicates the presence of elements such as Fe from the steel counterface, however the contribution from the underlying Al-based anodic oxide is still predominant, indicating that the iron oxide spots are very thin. Both the iron oxide distribution and the morphology of wear tracks on ECO coatings was not affected by the sealing post-treatment: the anodic oxide always undergoes mild micro-polishing. The slightly lower values of COF measured for sealed ECO are most likely related to the presence of the P-rich superficial layer on the surface of the sealed coating, since in this case iron oxides do not play a significant role in the contact.

On the surface of HA and PEO wear tracks, also light grey areas due to localised coating damage were observed (Fig. 9). These delamination spots appear already at 5 N on HA, whilst the presence of a thicker and more continuous transfer layer makes them less obvious on PEO, where they are clearly visible only at 40 N.

FIB cross-sections were prepared after sliding (Fig. 11) for a better understanding of subsurface coating damage occurring underneath the iron oxide-based transfer layers. In particular, ECO coatings retained their dense and compact microstructure during sliding, with no obvious crack formation and no detachment of hard wear debris due to brittle failure. Thin and compacted iron oxide patches are visible in places. Conversely, HA and PEO were covered by relatively thick iron oxide transfer layers and exhibited several cracks, both in transfer layers and through the thickness of the anodic oxide. The propagation and interconnection of these cracks eventually leads to coating detachment and failure, in the form of delamination spots as those observed in optical images of Figure 9.

#### 4. Conclusions

Microstructural and micro-mechanical characterization of anodic layers grown on the wrought AA6082-T5 alloy by industrial processes (hard anodizing (HA), plasma electrolytic oxidation (PEO) and electro-chemical oxidation (ECO), derived from PEO minimising its disruptive plasma discharge) was carried out and related to dry sliding behaviour (vs. 100Cr6 steel). The following conclusions can be drawn from this work:

- PEO and HA do not decrease the coefficient of friction of AA6082, whilst ECO does (particularly after sealing with a phosphate-based solution), thanks to its smooth surface and decreased stability of Fe-O based transfer layers.
- All the anodizing treatments improve wear resistance of AA6082. ECO layers showed the highest wear resistance, due to their beneficial combination of compact microstructure, high and uniform thickness, high microhardness and adhesion. Micro-cracking is a dominant wear mechanism in PEO and HA, leading to lower wear resistance by comparison to ECO.

These results show that the ECO treatment allows a further improvement by comparison to PEO and HA. In fact, ECO is carried out at high voltage and high energy density (at PEO level) but it reduces the detrimental effects of micro-discharges, thus producing smooth, hard and dense crystalline layers without some of the main drawbacks of PEO (e.g. high roughness and porosity).

#### Acknowledgements

This research did not receive any specific grant from funding agencies in the public, commercial, or not-for-profit sectors.

#### References

- [1] J. Gilbert Kaufman, Introduction to Aluminum Alloys and Tempers, ASM International, Materials Park, OH (USA), 2000, p. 87
- [2] S. Shrestha, B.D. Dunn, Plasma electrolytic oxidation and anodising of aluminium alloys for spacecraft applications, in: H. Dong (Ed.), Surface Engineering of Light Alloys - Al, Mg and Ti Alloys, Woodhead Publishing Ltd (2010) p. 603



- [3] C.M. Cotell, J.A. Sprague, F.A. Smidt, Jr. (Eds), Surface Engineering of Aluminum and Aluminum Alloys, ASM Handbook, Volume 5: Surface Engineering (1994) pp. 784-804. doi: 10.31399/asm.hb.v05.a0001308
- [4] A.L. Yerokhin, X. Nie, A. Leyland, A. Matthews, S.J. Dowey, Plasma electrolysis for surface engineering, Surface and Coatings Technology. 122 (1999) 73–93, doi: 10.1016/S0257-8972(99)00441-7
- [5] L. Rama Krishna, A. Sudha Purnima, G. Sundararajan, A comparative study of tribological behavior of microarc oxidation and hard-anodized coatings, Wear. 261 (2006) 1095–1101. doi:10.1016/j.wear.2006.02.002
- [6] U. Malayoglu, K. C. Tekin, U. Malayoglu, S. Shrestha, An investigation into the mechanical and tribological properties of plasma electrolytic oxidation and hard-anodized coatings on 6082 aluminum alloy, Materials Science and Engineering A. 528 (2011) 7451– 7460. doi:10.1016/j.msea.2011.06.032
- [7] J. M. Wheeler, J.A. Curran, S. Shrestha, Microstructure and multi-scale mechanical behavior of hard anodized and plasma electrolytic oxidation (PEO) coatings on aluminum alloy 5052, Surface & Coatings Technology. 207 (2012) 480–488. doi: 10.1016/j.surfcoat.2012.07.056
- [8] A. Algahtani, E.R.I. Mahmoud, S.Z. Khan, V. Tirth, Experimental Studies on Corrosion Behavior of Ceramic Surface Coating using Different Deposition Techniques on 6082-T6 Aluminum Alloy, Processes. 6, 240 (2018) 1-18. doi:10.3390/pr6120240
- [9] B.L. Jiang, Y.M. Wang, Plasma electrolytic oxidation treatment of aluminium and titanium alloys, in: H. Dong (Ed.), Surface Engineering of Light Alloys - Al, Mg and Ti Alloys, Woodhead Publishing Ltd (2010) p.110-154. doi: 10.1533/9781845699451.2.110
- [10] R.O. Hussein, D.O. Northwood, J.F. Su, X. Nie, A study of the interactive effects of hybrid current modes on the tribological properties of a PEO (plasma electrolytic oxidation) coated AM60B Mg-alloy, Surface & Coatings Technology. 215 (2013) 421–430. Doi:10.1016/j.surfcoat.2012.08.082
- [11] A.B. Rogov, A. Matthews, A. Yerokhin, Role of cathodic current in plasma electrolytic oxidation of Al: A quantitative approach to in-situ evaluation of cathodically induced effects, Electrochimica Acta. 317 (2019) 221-231. doi: 10.1016/j.electacta.2019.05.161
- [12] UNI EN 573-3 Aluminium and aluminium alloys - Chemical composition and form of wrought products - Part 3: chemical composition and form of products
- [13] Wenbin Xue, Zhiwei Deng, Yonchun Lai, Ruyi Chen, Analysis of Phase Distribution for Ceramic Coatings Formed by Microarc Oxidation on Aluminum Alloy, J. Am. Ceram. Soc. 81, (1998) 1365–68. doi not available
- [14] ASTM G77 -17, Standard Test Method for Ranking Resistance of Materials to Sliding Wear Using Block-on-Ring Wear Test, (2017). doi:10.1520/G0077-17
- [15] I. Boromei, L. Ceschini, A. Marconi, C. Martini, A duplex treatment to improve the sliding behavior of AISI 316L: Low-temperature carburizing with a DLC (a-C: H) topcoat, Wear. 302 (2013) 899–908. doi:10.1016/j.wear.2013.01.086
- [16] J.A. Williams, R.S. Dwyer-Joyce, Contact between solid surfaces, in: B. Bhushan (Ed.) Modern Tribology Handbook, CRC Press LLC, Boca Raton, Florida, USA (2000) pp.121–62
- [17] ISO 4287-2:1984. Surface roughness — Terminology — Part 2: Measurement of surface roughness parameters
- [18] J.A. Curran, T.W. Clyne, Thermo-physical properties of plasma electrolytic oxide coatings on aluminium, Surface & Coatings Technology. 199 (2005) 168–176. doi:10.1016/j.surfcoat.2004.09.037
- [19] G. Paternarakis, Development of a theory for the determination of the composition of the anodizing solution inside the pores during the growth of porous anodic Al<sub>2</sub>O<sub>3</sub> films on aluminium by a transport phenomenon analysis, Journal of Electroanalytical Chemistry. 447 (1998) 25–41 – doi not available



- [20] A. Yerokhin, R.H.U. Khan, Anodising of light alloys, in: H. Dong (Ed.), Surface Engineering of Light Alloys - Al, Mg and Ti Alloys, Woodhead Publishing Ltd (2010) p. 603. <https://doi.org/10.1533/9781845699451.2.83>
- [21] G. Sundararajan, L. Rama Krishna, Mechanisms underlying the formation of thick alumina coatings through the MAO coating technology, Surface and Coatings Technology. 167 (2003) 269–277. doi:10.1016/S0257-8972(02)00918-0;
- [22] R. Arrabal, Characterization and wear behaviour of PEO coatings on 6082-T6 aluminium alloy with incorporated  $\alpha$ -Al<sub>2</sub>O<sub>3</sub> particles, Surface & Coatings Technology. 269 (2015) 64–73. <http://dx.doi.org/10.1016/j.surfcoat.2014.10.048>
- [23] S. Lamouri, M. Hamidouche, N. Bouaouadja, H. Belhouichet, V. Garnier, G. Fantozzi, J.F. Trelkat, Control of the  $\gamma$ -alumina to  $\alpha$ -alumina phase transformation for an optimized alumina densification, Boletín de la Sociedad Española de Cerámica y Vidrio. 56 (2017) 47–54. <http://dx.doi.org/10.1016/j.bsecv.2016.10.001>
- [24] X. Nie, A. Leyland, H.W. Song, A.L. Yerokhin, S.J. Dowey, A. Matthews, Thickness effects on the mechanical properties of micro-arc discharge oxide coatings on aluminium alloys. Surface and Coatings Technology 116–119 (1999) 1055–1060, [https://doi.org/10.1016/S0257-8972\(99\)00089-4](https://doi.org/10.1016/S0257-8972(99)00089-4)
- [25] R.O. Ferreira, G.B. Galvani, I.S. Tertuliano, A.C.P. Rodrigues, C.R.F. Azevedo, Characterization and evolution of the coefficient of friction during pin on disc tribotest: Comparison between C10200Cu, AA6082-T6 Al and C36000 brass pins under varying normal loads, Tribology International 138 (2019), 403–414, <https://doi.org/10.1016/j.triboint.2019.06.013>
- [26] Ruiz-Andrés M, Conde A, de Damborenea J, Garcia I. Wear behavior of aluminum alloys at slow sliding speeds. TribolTrans, 2015; 58:955–62., <https://doi.org/10.1080/10402004.2015.1027432>
- [27] Menezes P. L., V. Kailas S. Influence of surface texture and roughness parameters on friction and transfer layer formation during sliding of aluminium pin on steel plate, Wear, vol.267., 2009., p.1534–49. <https://doi.org/10.1016/j.wear.2009.06.003>
- [28] Prakash NA, Gnanamoorthy R, Kamaraj M. Friction and wear behavior of surface nanocrystallized aluminium alloy under dry sliding condition. Mater. Sci. EngB 2010; vol. 168:176–81, <https://doi.org/10.1016/j.mseb.2009.11.011>
- [29] G.W. Stachowiak, A.W. Batchelor, Engineering Tribology, 3rd ed., Elsevier Butterworth-Heinemann, Oxford, 2005, pp. 484–485
- [30] G. Sabatini, L. Ceschini, C. Martini, J.A. Williams, I.M. Hutchings, Improving sliding and abrasive wear behaviour of cast A356 and wrought AA7075 aluminium alloys by plasma electrolytic oxidation, Materials & Design. 31 (2010) 816–828. doi:10.1016/j.matdes.2009.07.053
- [31] L. Tonelli, L. Pezzato, P. Dolcet, M. Dabalà, C. Martini, Effects of graphite nano-particle additions on dry sliding behaviour of plasma-electrolytic-oxidation-treated EV31A magnesium alloy against steel in air, Wear. 404–405, (2018) 2012–2022, <https://doi.org/10.1016/j.wear.2018.03.012>
- [32] C. Martini, L. Ceschini, F. Tarterini, J.M. Paillard, J.A. Curran, PEO layers obtained from mixed aluminate–phosphate baths on Ti–6Al–4V: Dry sliding behaviour and influence of a PTFE topcoat, Wear. 269 (2010) 747–756, <https://doi.org/10.1016/j.surfcoat.2016.05.001>
- [33] S. Wilson, A.T. Alpas, TiN coating wear mechanisms in dry sliding contact against high speed steel, Surf. Coat. Technol. 108–109 (1998) 369–376, [https://doi.org/10.1016/S0257-8972\(98\)00593-3](https://doi.org/10.1016/S0257-8972(98)00593-3)
- [34] J.L. Sullivan, S.G. Hodgson, A study of mild oxidational wear for conditions of low load and speed, Wear. 121 (1988) 95–106, [https://doi.org/10.1016/0043-1648\(88\)90033-6](https://doi.org/10.1016/0043-1648(88)90033-6)

## Captions

**Table 1:** Chemical composition of AA6082 (wt.%): comparison of measured data (GDOES) with nominal data (UNI EN 573-3 [12]).

**Table 2:** Main features of the industrial anodizing treatments.

**Table 3:** Maximum and mean Hertzian contact pressures on untreated and anodized AA6082-T5 as a function of normal load (dry sliding against AISI 52100).

**Table 4:** Surface roughness parameters according to ISO 4278 [17] for the AA6082 substrate and for anodized samples, together with average thickness values of anodic oxides (with relative standard deviation values, RSD).

**Table 5:** Chemical composition (EDS, wt.%) of debris layers on wear tracks obtained at 20 N after dry sliding against 100Cr6 steel (1000 m, 0.3 m/s).

**Figure 1:** Secondary electron (SE) images of the free surface morphology (a-c) and backscattered electron (BSE) images of polished cross-sections (d-n) of AA6082-T5 anodized by HA, PEO and ECO processes.

**Figure 2:** EDS X-ray maps of polished cross-sections of AA6082-T5 anodized by HA, PEO and ECO processes. Also the sealed version of the ECO layer is shown in the right-hand column.

**Figure 3:** Indexed  $\theta$ - $2\theta$  X-ray diffraction patterns, representative of the through thickness phase constitution of PEO layers in the as-treated condition (PEO, ECO, HA processes).

**Figure 4:** Cross-sectional Knoop indentation profiles of PEO, HA, ECO and ECO sealed samples.

**Figure 5:** Progressive load scratch test:  $L_{c2}$  values (a) and 3D-digital optical micrographs (b) of scratch tracks on PEO, HA, ECO and ECO sealed samples.

**Figure 6:** Dry sliding tests: coefficient of friction vs sliding distance of untreated AA6082, PEO, HA, ECO and ECO sealed samples (under 5 N normal load).

**Figure 7:** Dry sliding tests: coefficient of friction vs normal load for untreated AA6082, PEO, HA, ECO and ECO sealed samples.

**Figure 8:** Dry sliding tests: maximum wear depth vs normal load. Global comparison among untreated AA6082 and anodised samples (a); enlarged section with data of anodised samples (b).

**Figure 9:** Dry sliding tests: 3D-digital microscopy images of wear tracks. The white arrows indicate light grey areas in which the substrate becomes visible due to coating damage.

**Figure 10:** Dry sliding tests: SEM images of worn surfaces of (a) PEO, (b) HA, (c) ECO and (d) ECO sealed

**Figure 11:** Dry sliding tests: FIB cross-sections images (FEG-SEM) of wear scars on anodic oxide layers obtained at 40 N. The interface between residual coating and substrate is highlighted by white dashed lines. The white arrow indicates the compact transfer layer on the surface of the worn ECO coating.

Color should not be used for any figures in print.

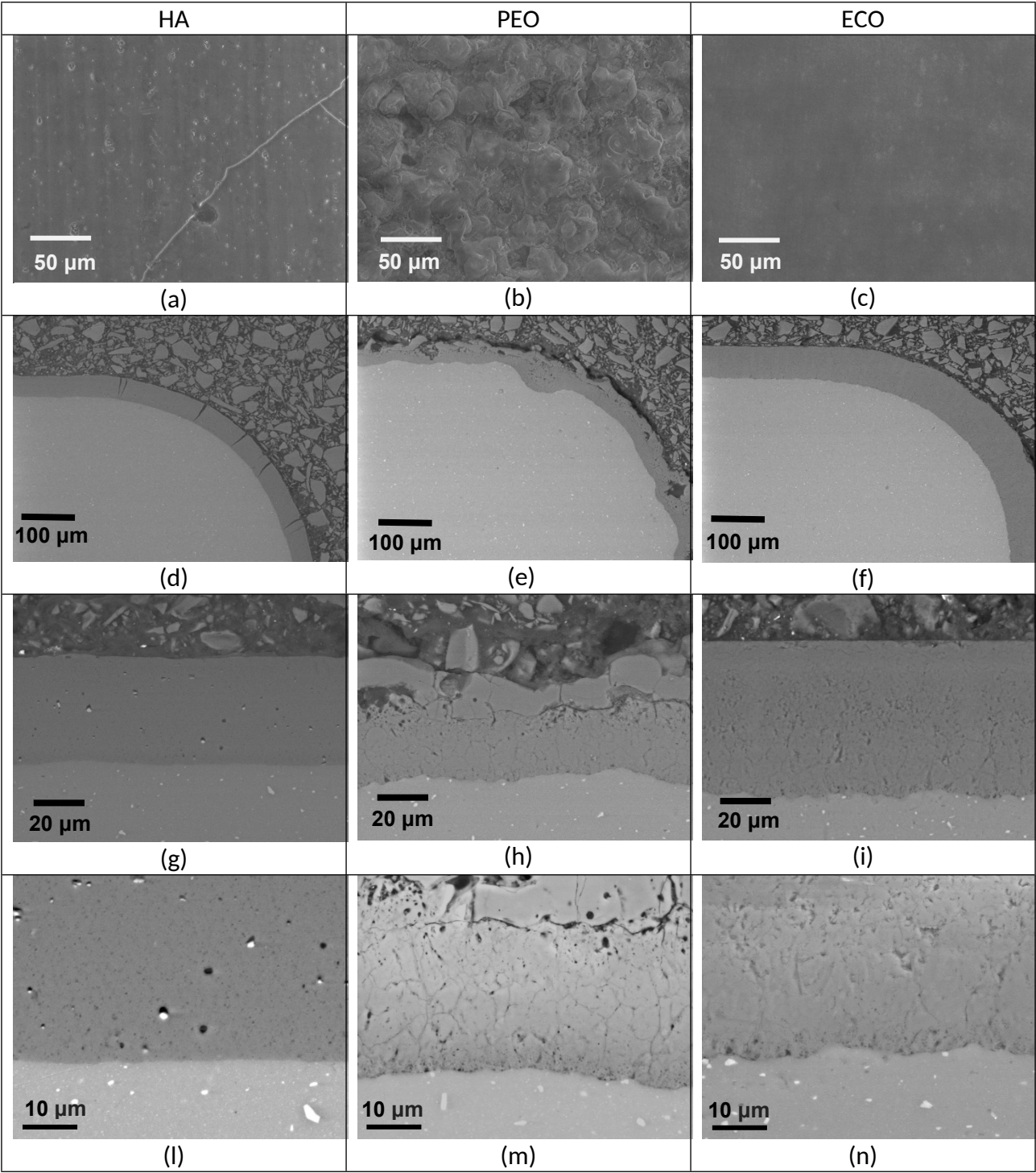


**Figure 1:** Secondary electron (SE) images of the free surface morphology (a-c) and backscattered electron (BSE) images of polished cross-sections (d-n) of AA6082-T5 anodized by HA, PEO and ECO processes.

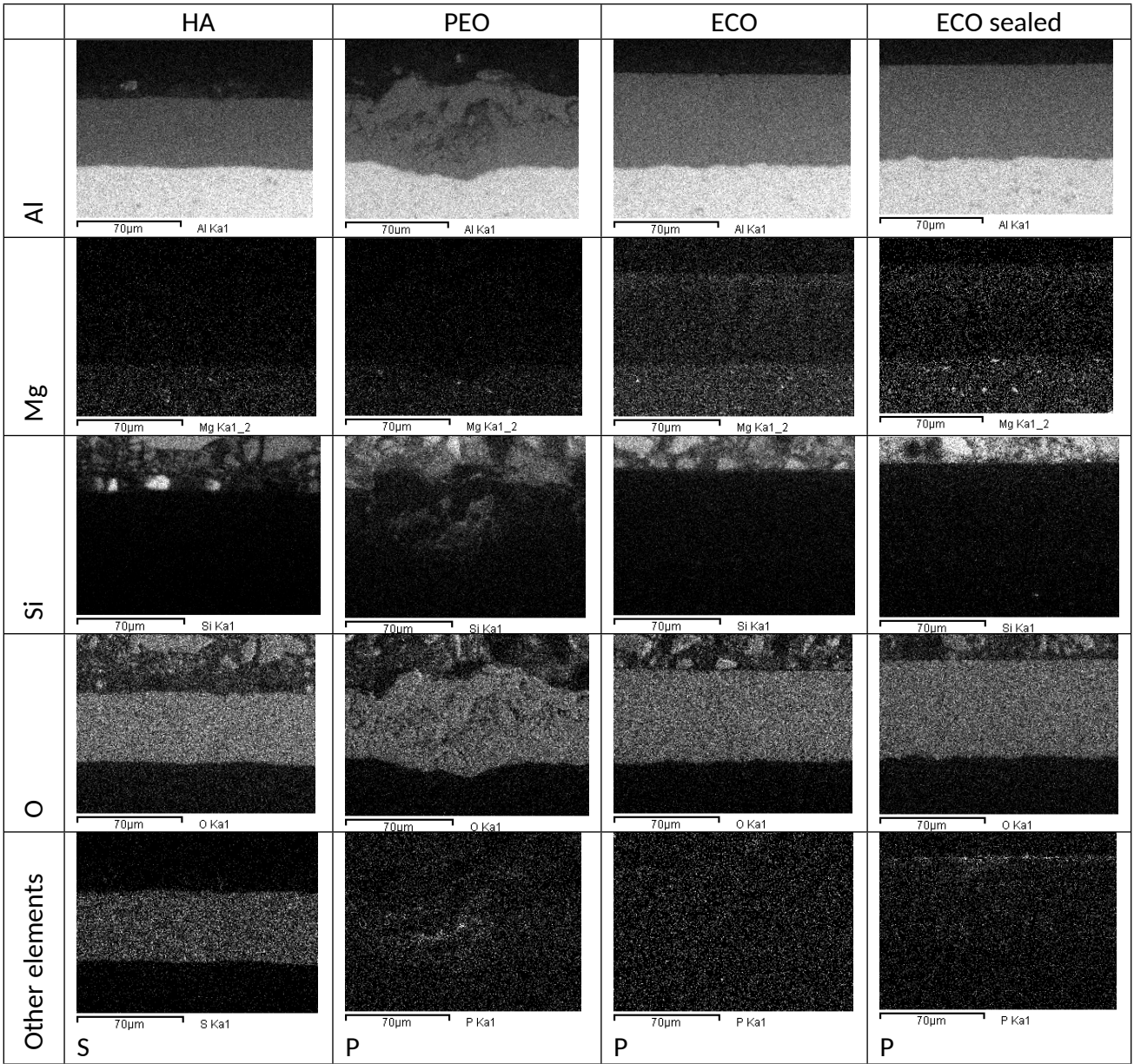


**Figure 2:** EDS X-ray maps of polished cross-sections of AA6082-T5 anodized by HA, PEO and ECO processes. Also the sealed version of the ECO layer is show in the right-hand column.

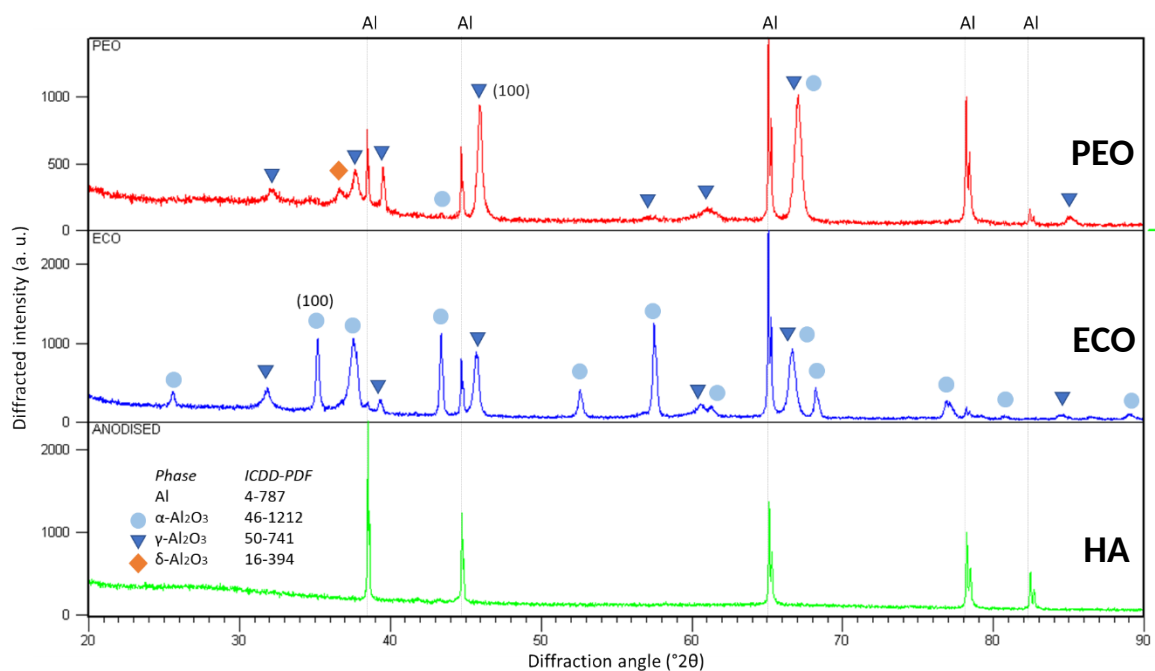


**Figure 3:** Indexed  $0-2\theta$  X-ray diffraction patterns, representative of the through thickness phase constitution of PEO layers in the as-treated condition (PEO, ECO, HA processes).



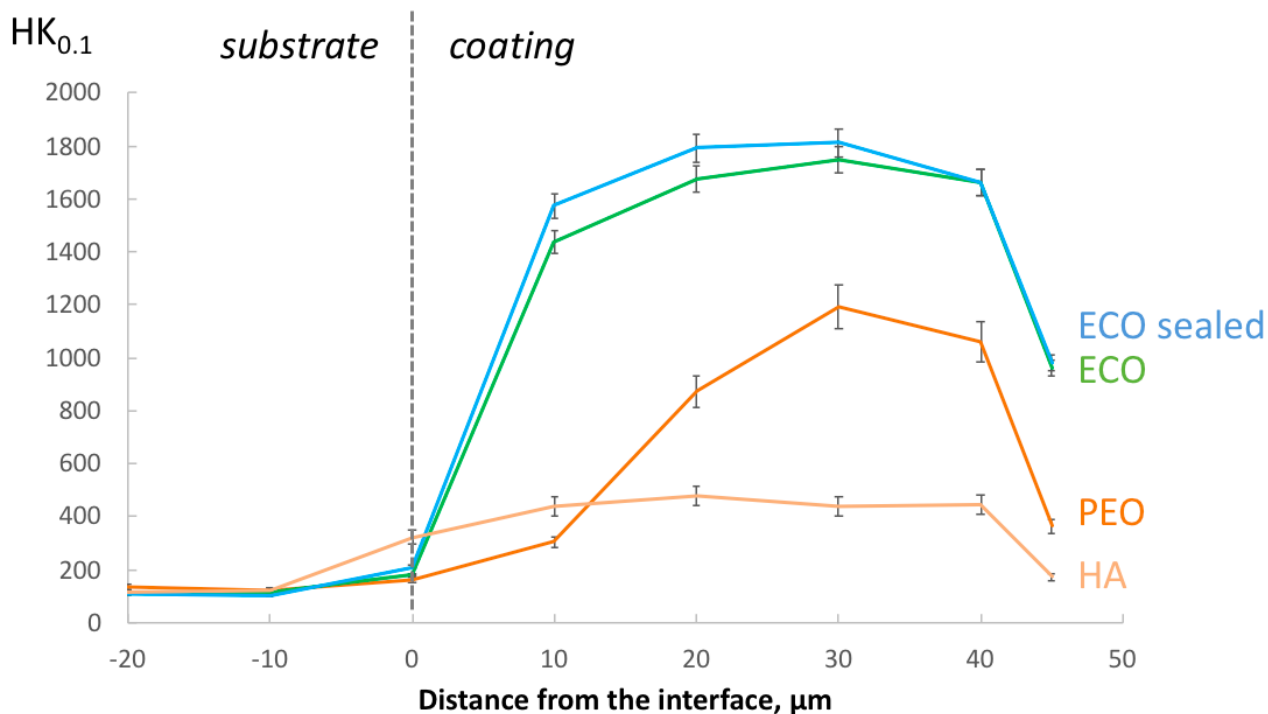


**Figure 4:** Cross-sectional Knoop indentation profiles of PEO, HA, ECO and ECO sealed samples.

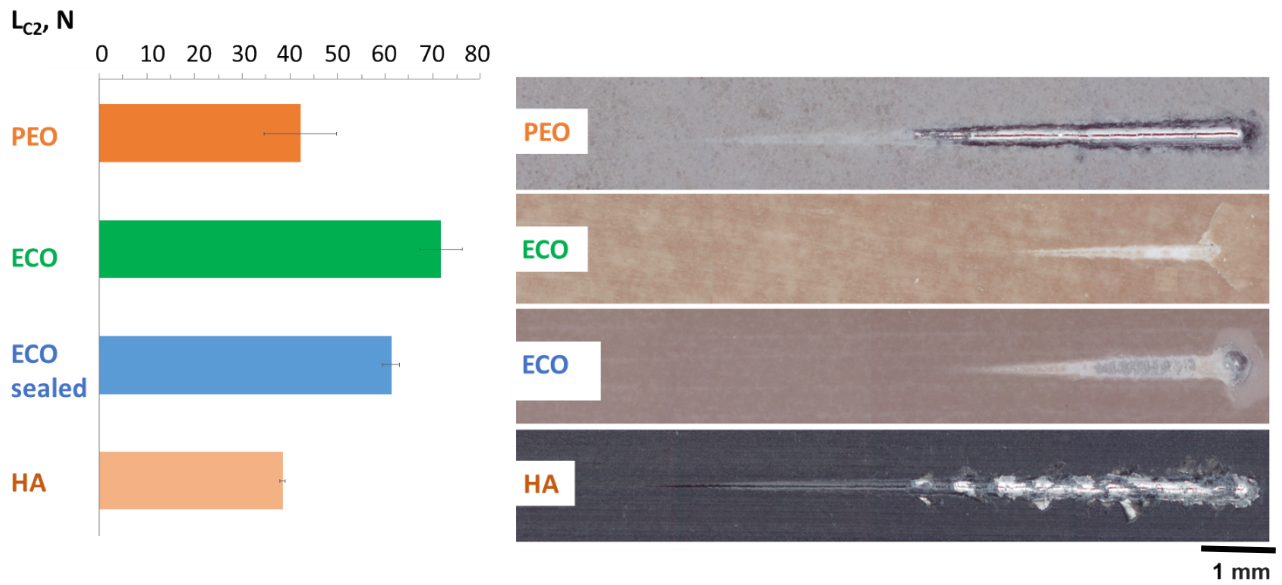


**Figure 5:** Progressive load scratch test:  $L_{c2}$  values (a) and 3D-digital optical micrographs (b) of scratch tracks on PEO, HA, ECO and ECO sealed samples.



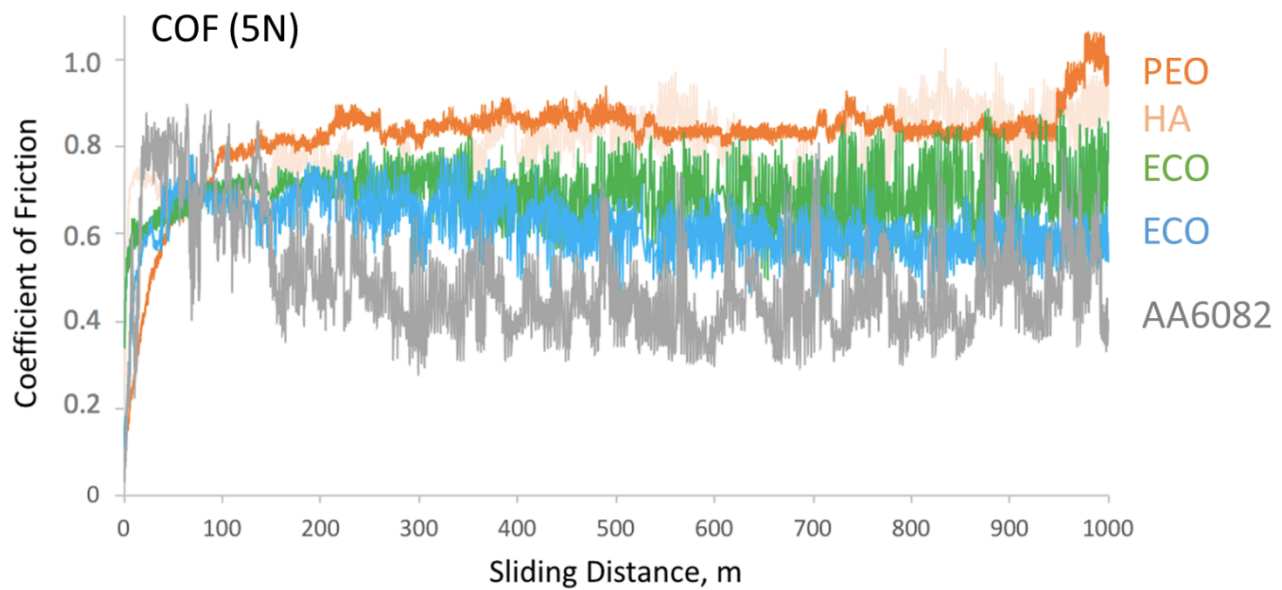


**Figure 6:** Dry sliding tests: coefficient of friction vs sliding distance of untreated AA6082, PEO, HA, ECO and ECO sealed samples (under 5 N normal load).

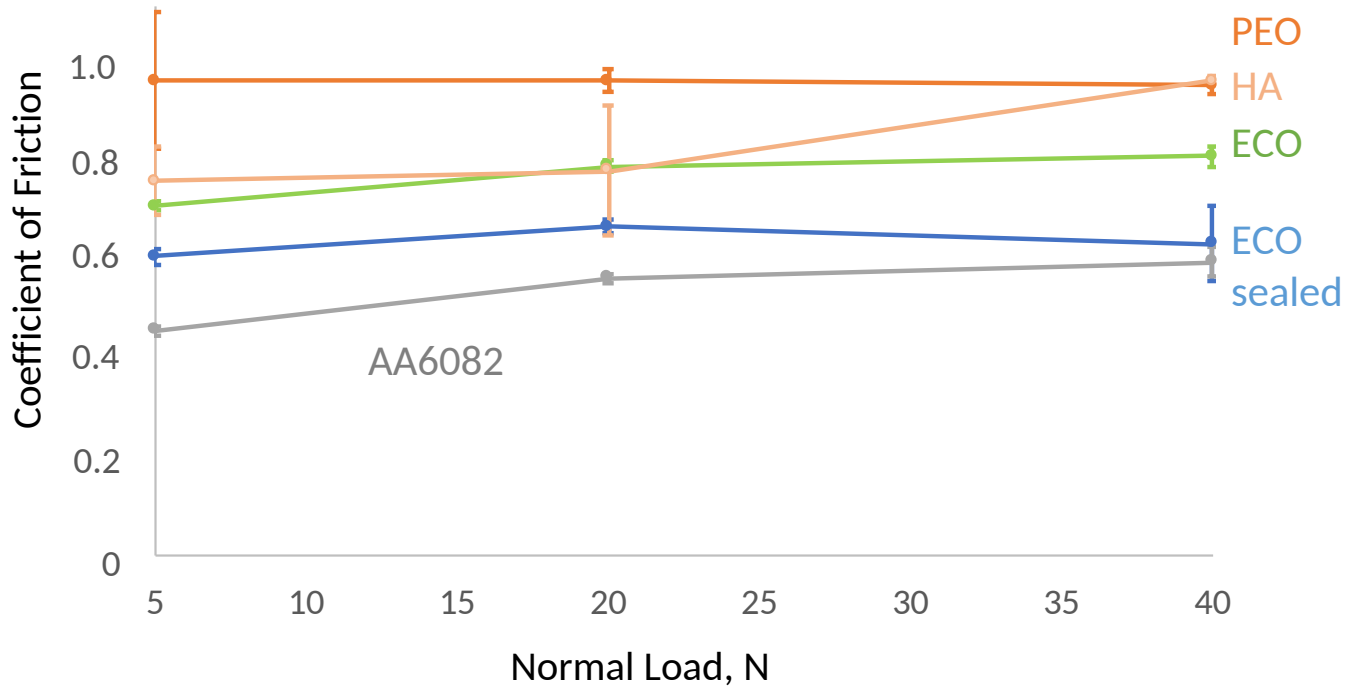
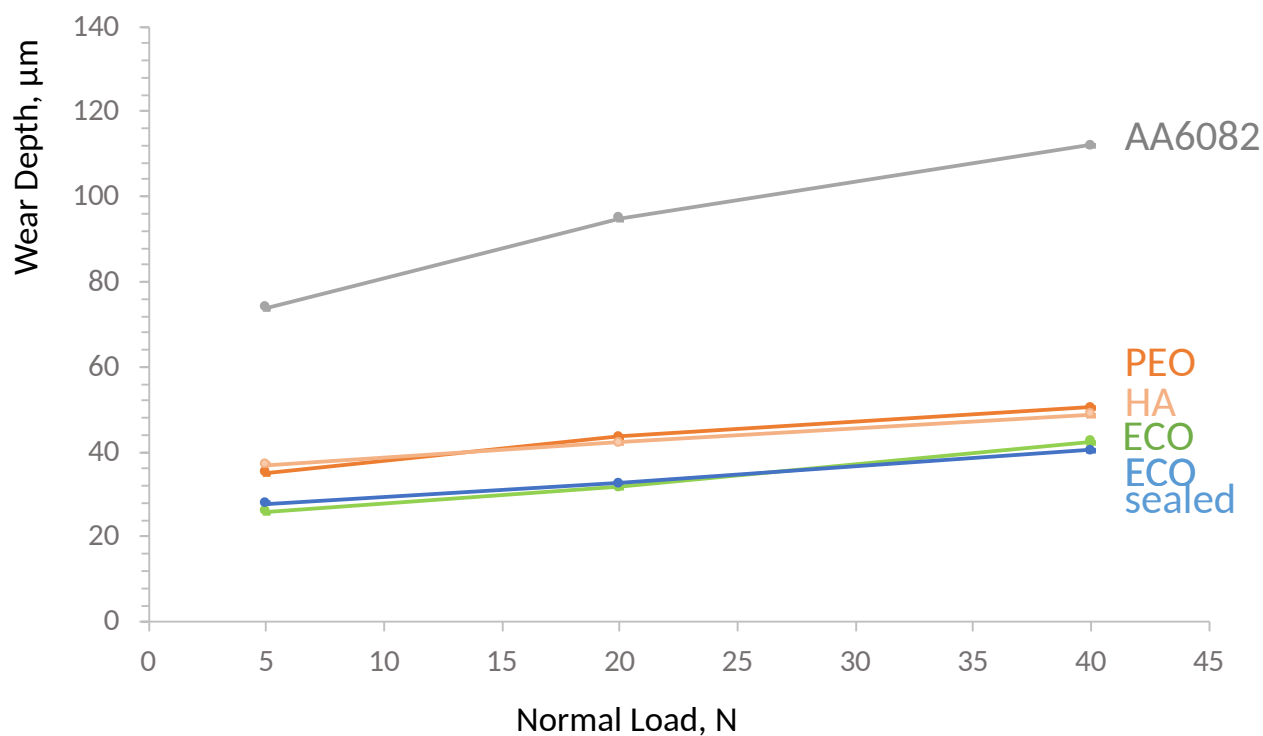
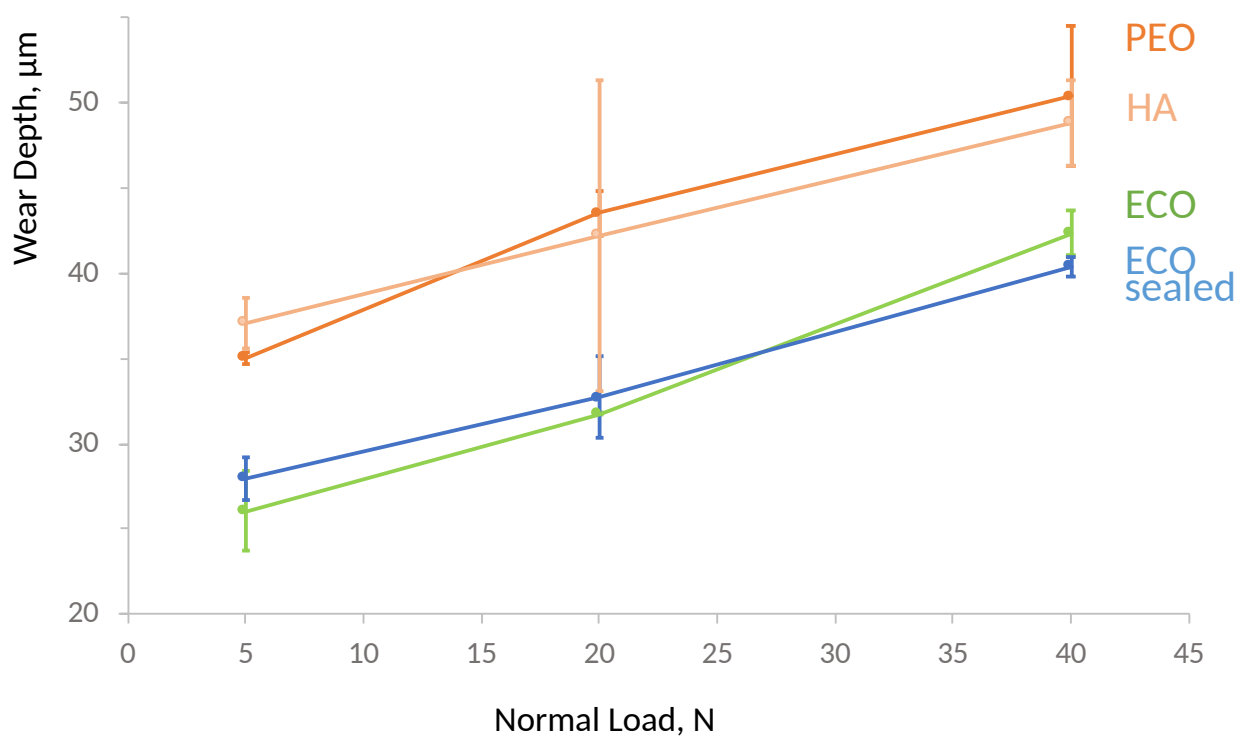


**Figure 7:** Dry sliding tests: coefficient of friction vs normal load for untreated AA6082, PEO, HA, ECO and ECO sealed samples.



(a)



(b)

**Figure 8:** Dry sliding tests: maximum wear depth vs normal load. Global comparison among untreated AA6082 and anodised samples (a); enlarged section with data of anodised samples (b).

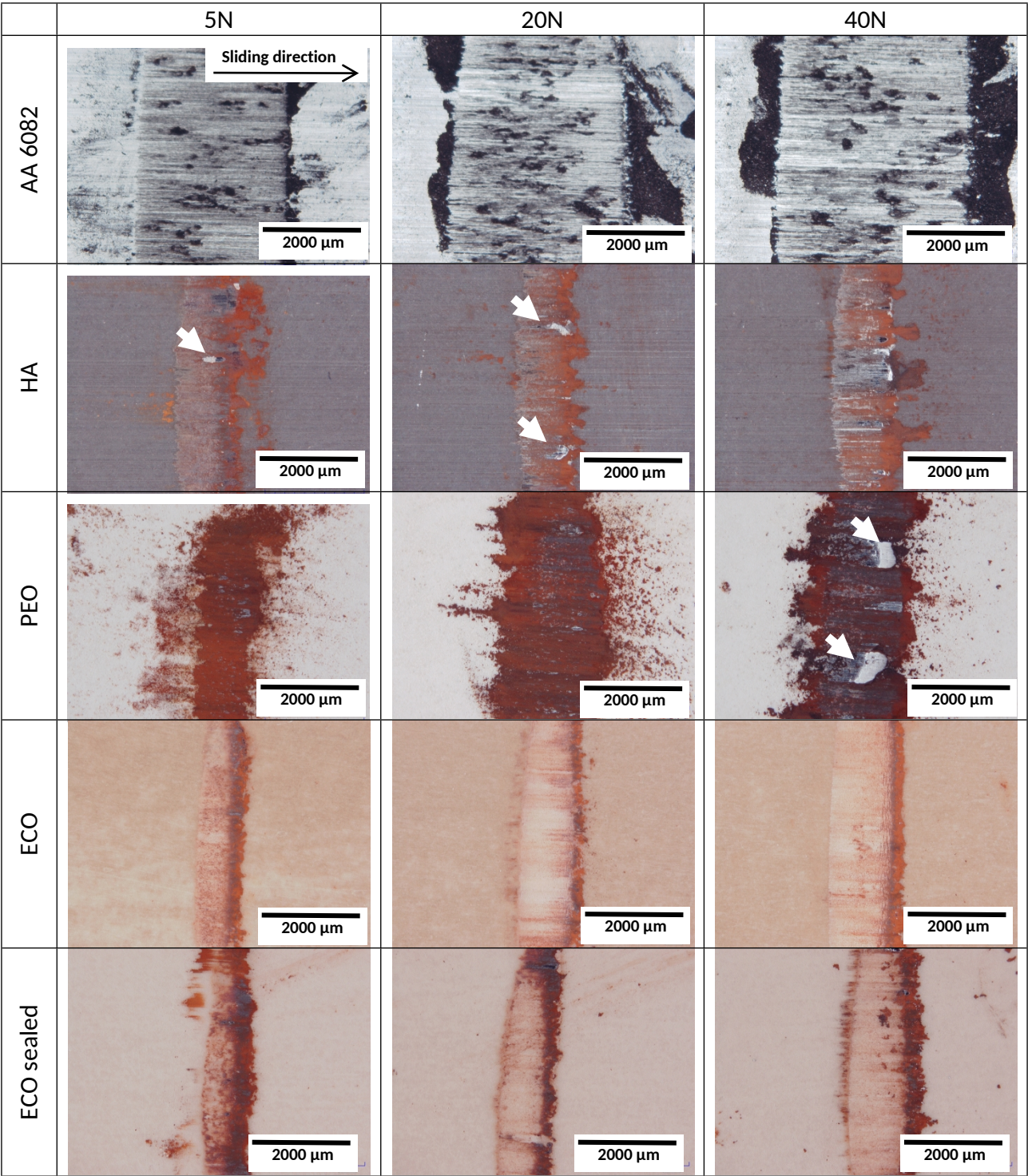


**Figure 9:** Dry sliding tests: 3D-digital microscopy images of wear tracks. The white arrows indicate light grey areas in which the substrate becomes visible due to coating damage.



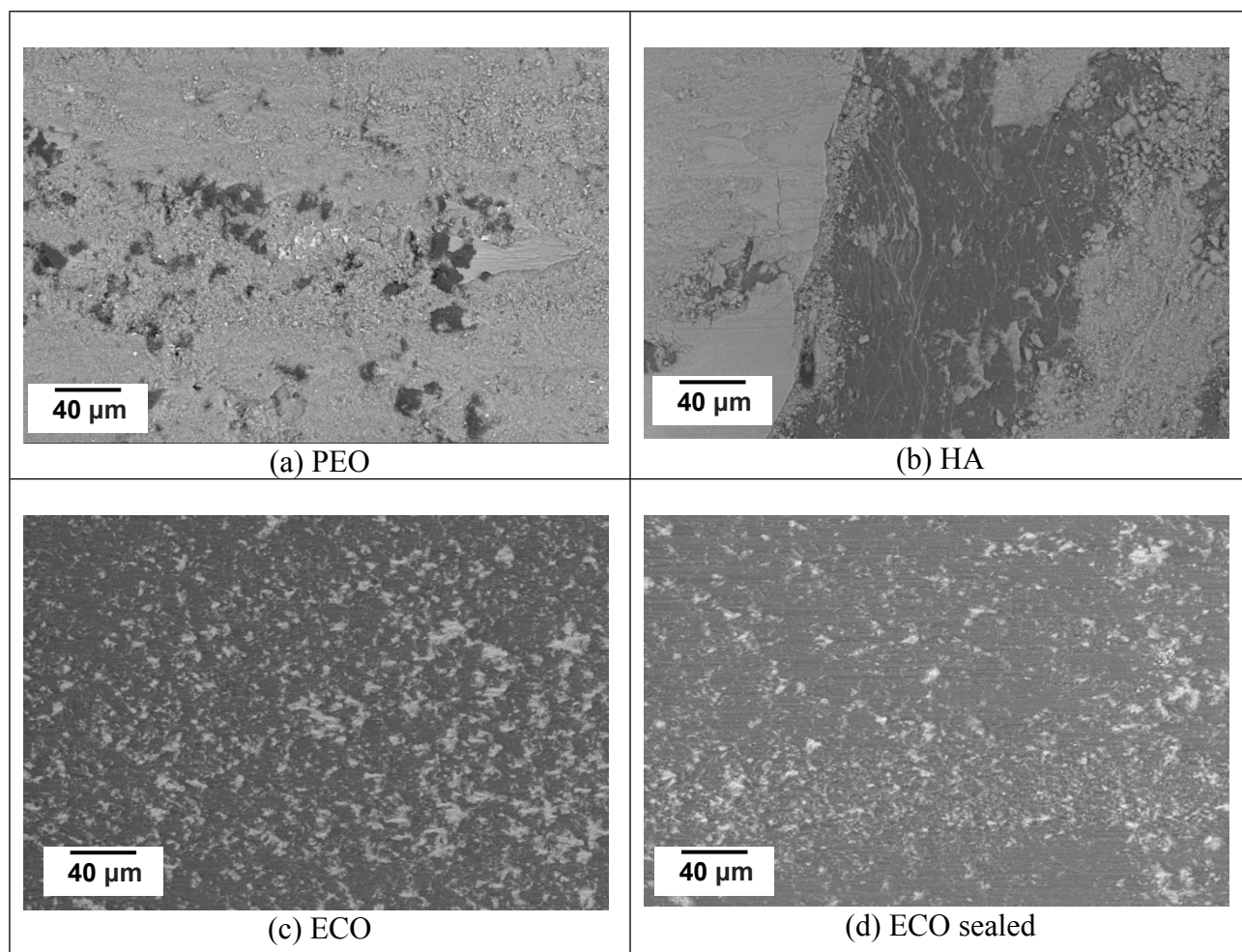


**Figure 10:** Dry sliding tests: SEM images of worn surfaces of (a) PEO, (b) HA, (C) ECO and (D) ECO sealed

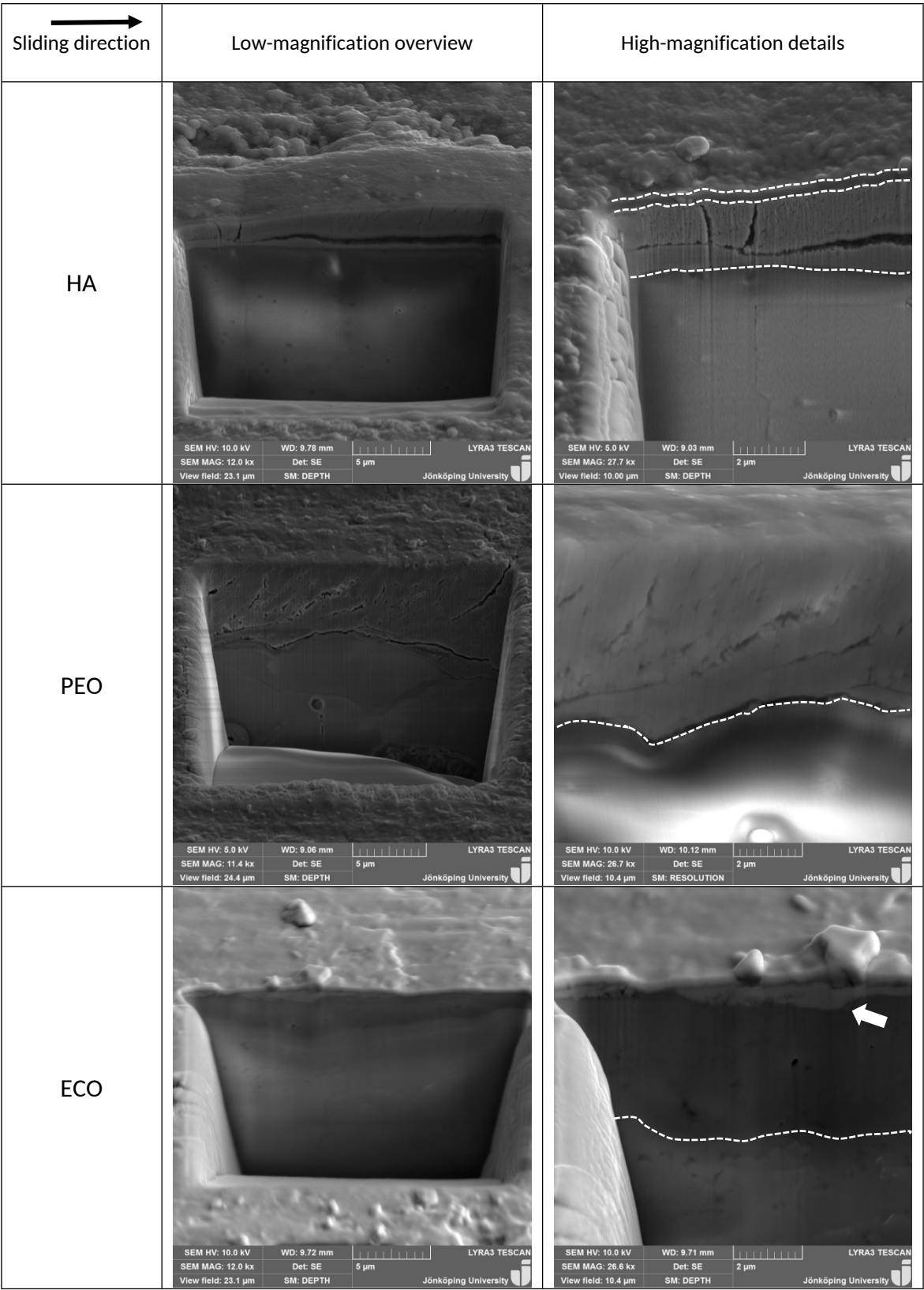


**Figure 11:** Dry sliding tests: FIB cross-sections images (FEG-SEM) of wear scars on anodic oxide layers obtained at 40 N. The interface between residual coating and substrate is highlighted by white dashed lines. The white arrow indicates the compact transfer layer on the surface of the worn ECO coating.

## Tables

**Table 1:** Chemical composition of AA6082 (wt.%): comparison of measured data (GDOES) with nominal data (UNI EN 573-3).

wt. %	Cr	Cu	Fe	Mg	Mn	Si	Ti	Zn	Other
Measured	0.004±0.001	0.03±0.001	0.18±0.01	0.62±0.01	0.57±0.03	0.93±0.01	0.01±0.002	0.06±0.01	0.047
Nominal	max 0.25	max 0.10	max 0.50	0.6-1.2	0.40-1.0	0.7-1.3	max 0.10	max 0.20	0.05-0.15

**Table 2:** Main features of the industrial anodizing treatments.

Process	Voltage/Current density; Discharge effect	Energy consumption (kW h m <sup>-2</sup> μm <sup>-1</sup> )	Electrolyte	Process tank temperature	Electric equipment and conditions
PLASMA ELECTROLYTIC OXIDATION (PEO)	300-600 V/ 100-500 mA cm <sup>-2</sup> Micro-arc discharge	3-27	Dilute alkaline solution (Na <sub>2</sub> SiO <sub>3</sub> , Na <sub>4</sub> P <sub>2</sub> O <sub>7</sub> )	15-20° C	Square pulse power supply
ELECTRO-CHEMICAL OXIDATION (ECO)	400-700 V/ 200-500 mA cm <sup>-2</sup> Low-discharge oxidation	4-22	Colloidal alkaline solution (Al(OH) <sub>3</sub> , NaAlO <sub>2</sub> , Na <sub>4</sub> P <sub>2</sub> O <sub>7</sub> )	room T	Pulsed bipolar current (PBC) power supply
HARD ANODISING (HA)	15-160 V/ ≤ 50 mA cm <sup>-2</sup> Non-discharge oxidation	0.1-0.5	Concentrated acid (H <sub>2</sub> SO <sub>4</sub> )	< room T	DC rectifier

**Table 3:** Maximum and mean Hertzian contact pressures on untreated and anodized AA6082-T5 as a function of normal load (dry sliding against AISI 52100).

Contact pressure, MPa	5N		20N		40N	
	P <sub>max</sub>	P <sub>mean</sub>	P <sub>max</sub>	P <sub>mean</sub>	P <sub>max</sub>	P <sub>mean</sub>
untreated	22	17	43	34	61	48
PEO	31	24	62	49	88	69
ECO	33	26	65	51	92	73
HA	31	24	62	49	88	69



**Table 4:** Surface roughness parameters according to ISO 4278 for the AA6082 substrate and for anodized samples, together with average thickness values of anodic oxides (with relative standard deviation values, RSD).

	<b>Ra (μm)</b>	<b>Rq (μm)</b>	<b>Rz (μm)</b>	<b>Rmax (μm)</b>	<b>Rt (μm)</b>	<b>Thickness (μm)</b>
<b>AA6082 (untreated)</b>	0.91 ± 0.15	1.13 ± 0.19	5.17 ± 0.53	7.09 ± 0.40	8.28 ± 1.11	-
<b>HA</b>	0.91 ± 0.05	1.14 ± 0.05	5.67 ± 0.06	7.28 ± 0.24	7.55 ± 0.37	44.6 ± 0.5 (RSD 1.1%)
<b>PEO</b>	3.80 ± 0.06	4.7 ± 0.13	22.08 ± 1.43	27.05 ± 2.16	28.00 ± 2.16	43.1 ± 4.8 (RSD 11%)
<b>ECO</b>	0.18 ± 0.01	0.24 ± 0.01	1.36 ± 0.06	1.96 ± 0.18	2.08 ± 0.16	64.8 ± 1.0 (RSD 1.5%)
<b>ECO sealed</b>	0.19 ± 0.01	0.24 ± 0.01	1.29 ± 0.11	1.82 ± 0.08	1.93 ± 0.02	58.1 ± 0.5 (RSD 0.9%)

**Table 5:** Chemical composition (EDS, wt.%) of debris layers on wear tracks obtained at 20 N after dry sliding against 100Cr6 steel (1000 m, 0.3 m/s).

	<b>C</b>	<b>O</b>	<b>Mg</b>	<b>Al</b>	<b>P</b>	<b>Si</b>	<b>Cr</b>	<b>Mn</b>	<b>Fe</b>
<b>AA6082</b>	1.5	30.7	0.3	62.0	-	0.5	-	0.3	4.6
<b>HA</b>	2.3	44.8	-	-	-	-	0.4	0.1	52.3
<b>PEO</b>	2.5	35.9	-	-	-	-	0.9	-	60.8
<b>ECO</b>	2.4	50.0	1.1	41.0	-	-	-	0.8	4.8
<b>ECO sealed</b>	3.0	47.9	1.2	38.8	2.3	-	-	0.9	5.9